Supplementary Information

From Au-rich Core/PtNi-rich Shell to Ni-rich Core/PtAu-rich Shell: an Effective Thermochemical Pathway to Nanoengineering Catalysts for Fuel Cells

Aolin Lu[a,b], Zhipeng Wu[b], Binghui Chen[a], Dong-Liang Peng[a], Shan Yan[b], Shiyao Shan[b], Zakiya Skeete[b], Fangfang Chang[b], Yuanzhi Chen[a], Hongfei Zheng[a], Deqian Zeng[a], Lefu Yang[a], Anju Sharma[b], Jin Luo[b], Lichang Wang[c], Valeri Petkov[d], and Chuan-Jian Zhong[b]*

a) Department of Chemical and Biochemical Engineering, College of Chemistry and Chemical Engineering; and Department of Materials Science and Engineering, College of Materials, Xiamen University, Xiamen 361005, China.
b) Department of Chemistry, State University of New York at Binghamton, Binghamton, NY 13902, USA.
c) Department of Chemistry and Biochemistry, Southern Illinois University, Carbondale, Illinois 62901, USA.
d) Department of Physics, Central Michigan University, Mt. Pleasant, Michigan 48859, USA.
(* - Corresponding author, email: cjzhong@binghamton.edu)

Additional Experimental Results and Schematic Illustrations:

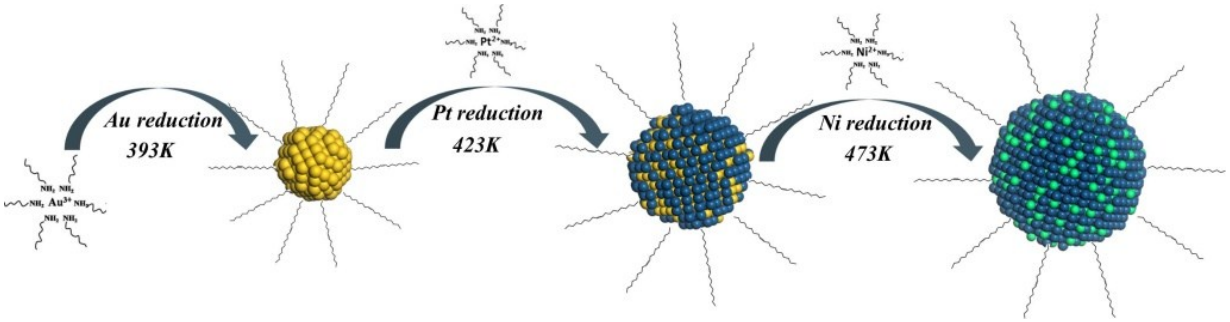

Scheme S1. A schematic illustration of the processes involved in the formation of Au@PtNi core-shell nanoparticles in the one-pot synthesis route.

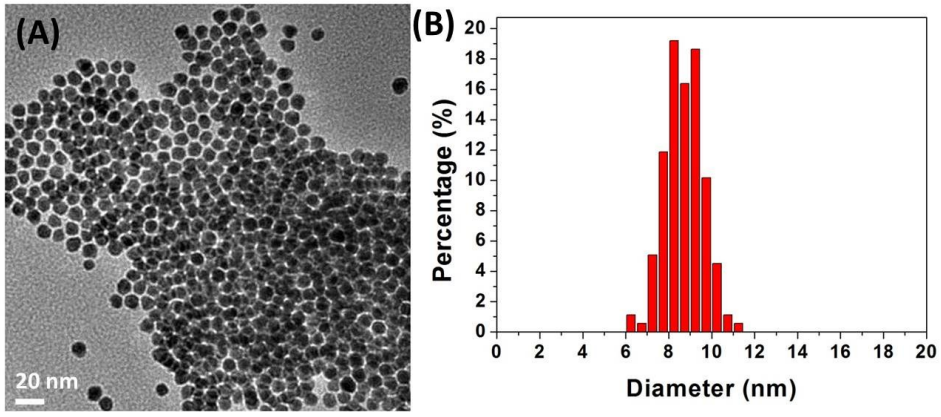

Figure S1. (A) TEM image of as synthesized $Pt_{39}Au_{18}Ni_{43}$ core-shell nanoparticles and (B) corresponding histogram of the size distribution.

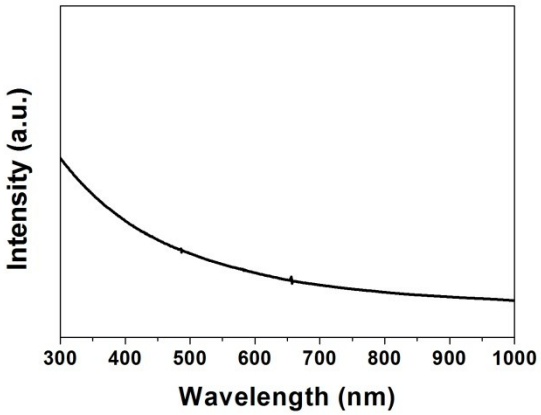

Figure S2. UV-vis spectrum of as-prepared $Pt_{39}Au_{18}Ni_{43}$ core-shell nanoparticles dispersed in hexane.

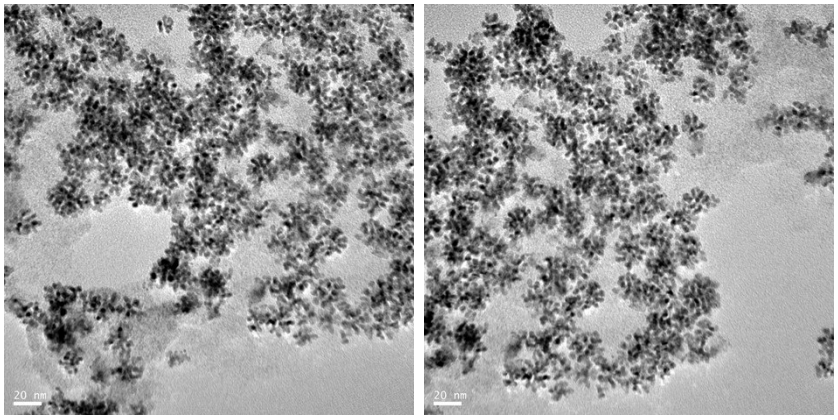

Figure S3. TEM images of as-synthesized $Pt_{32}Ni_{68}$ nanoflowers in two sampling regions.

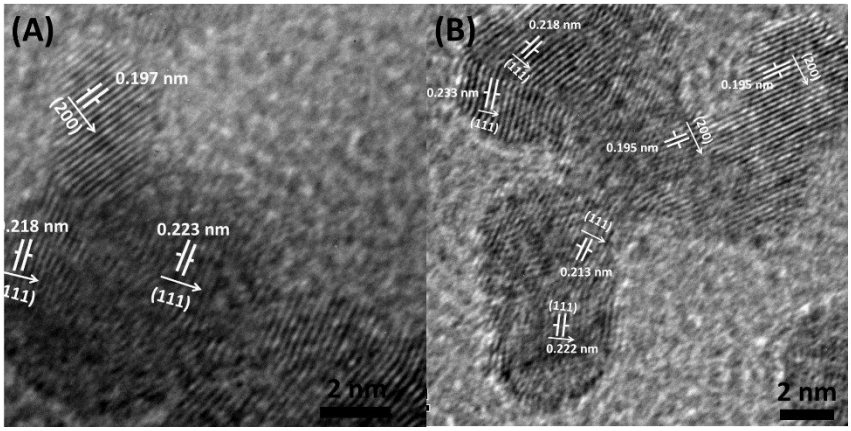

Figure S4. HR-TEM images of as-synthesized NPs, showing (A) short and (B) long branched $Pt_{37}Au_8Ni_{55}$.

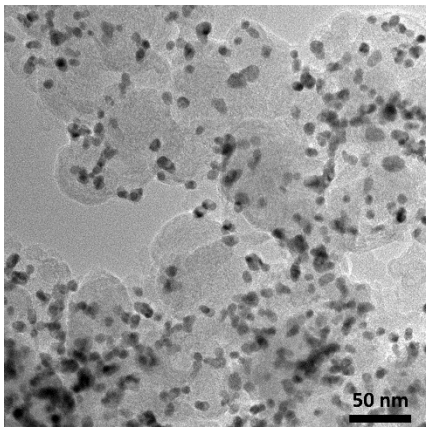

Figure S5. TEM image of 400 ºC/H_2 treated $Pt_{37}Au_8Ni_{55}$/C catalyst.

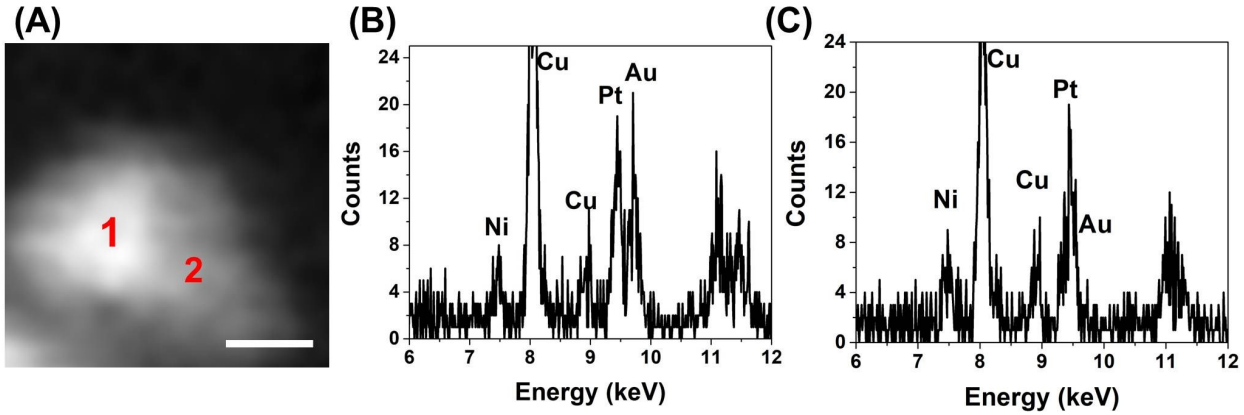

Figure S6. (A): HADDF-STEM image showing a sample region with Au-rich core/PtNi rich shell for the nanoparticles (scale bar: 5 nm); (B-C): EDS spectra showing the composition analyses (B) in the core (point 1) which has a composition of $Pt_{46}Au_{39}Ni_{15,}$ and (C) in shell zone which has a composition of $Pt_{64}Au_{10}Ni_{25}$ (point 2).

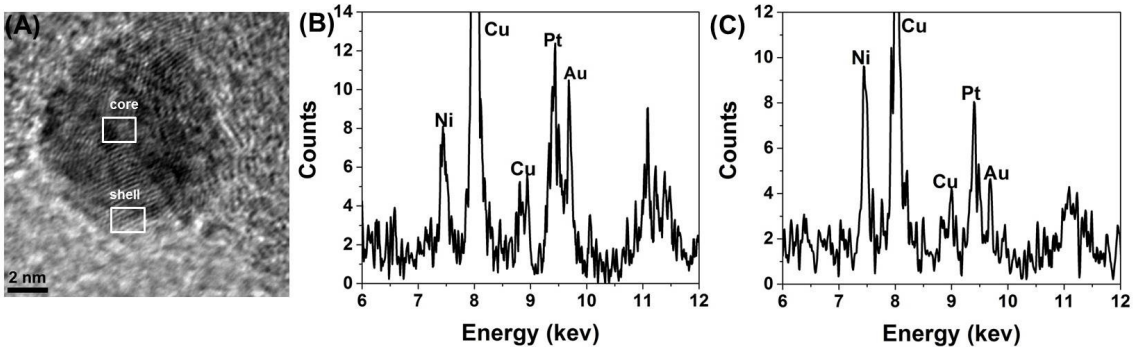

Figure S7. (A): HR-TEM image showing a single particle from a sample of the 260 ºC/O_2 treated $Pt_{39}Au_{18}Ni_{43}$/C; (B-C): EDS spectra showing the composition in the core (B) and (C) shell zone.

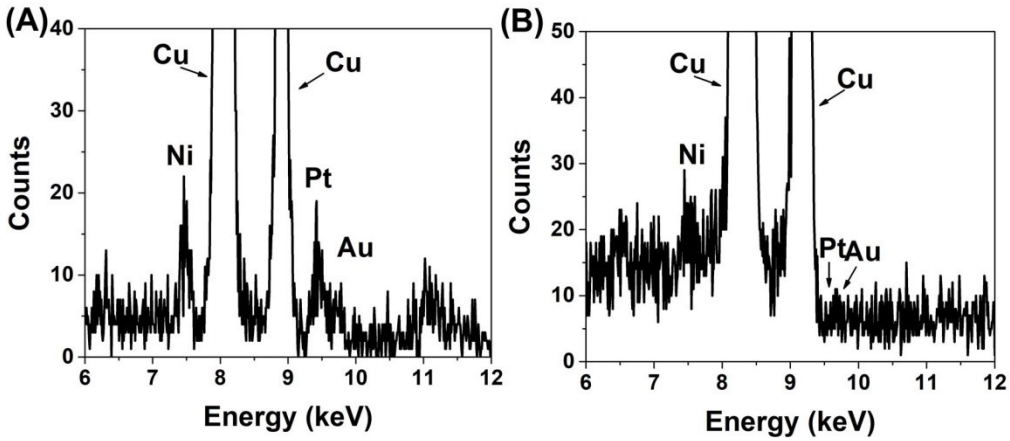

Figure S8 EDS spectra showing the bulk composition analysis ($Pt_{36}Au_{18}Ni_{46}$) and core point composition analysis ($Pt_{10}Au_5Ni_{85}$) in the red rectangle region of Figure 4A for the Ni-rich core and PtAu-rich shell nanoparticles.

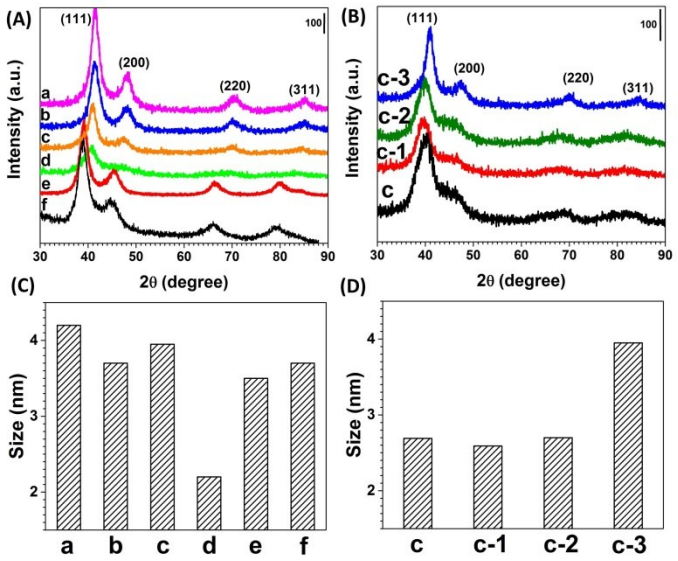

Figure S9. (A) XRD data of 400 ºC/H_2 treated (a) $Pt_{34}Au_2Ni_{64}$/C, (b) $Pt_{37}Au_8Ni_{55}$/C, (c) $Pt_{39}Au_{18}Ni_{43}$/C, (d) $Pt_{40}Au_{30}Ni_{30}$/C, (e) $Pt_{56}Au_{44}$/C, and (f) $Pt_{38}Au_{62}$/C. (B) XRD data of (c) as-synthesized, (c-1) 260 ºC/O_2, (c-2) 177 ºC/O_2, (c-3) 400 ºC/H_2 of $Pt_{39}Au_{18}Ni_{43}$/C (C) the grain sizes calculated from curves in (A), (D) the grain sizes calculated from curves in (B).

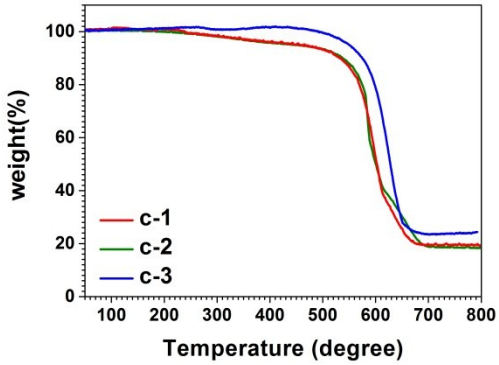

Figure S10. (a) TGA curves for (c-1) 260 ºC/O_2, (c-2) 177 ºC/O_2, and (c-3) 400 ºC/H_2 treated $Pt_{39}Au_{18}Ni_{43}$/C.

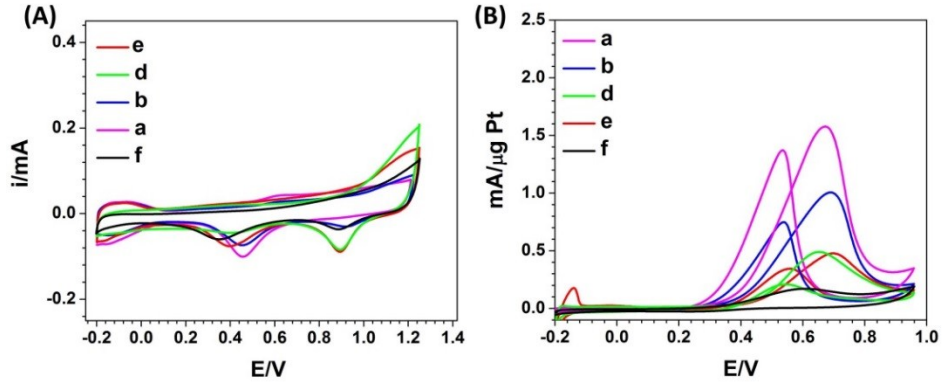

Figure S11. (A) CV curves and (B) MOR CV curves of 400 ºC/H_2 treated (a) $Pt_{34}Au_2Ni_{64}$/C, (b) $Pt_{37}Au_8Ni_{55}$/C, (d) $Pt_{40}Au_{30}Ni_{30}$/C, (e) $Pt_{56}Au_{44}$/C, and (f) $Pt_{38}Au_{62}$/C in 0.5 M CH_3OH+0.1 M $HClO_4$.

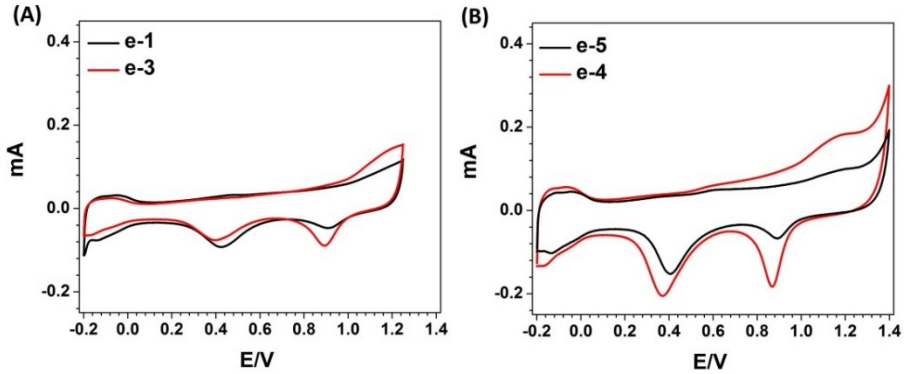

Figure S12. CV curves of $Pt_{56}Au_{44}$/C involves (e-1) 260 ºC/O_2 and (e-3) 400 ºC/H_2 treatment. Curve (e-4) and (e-5) involves e-3 and e-1 cycling to a higher potential (1.39 V).

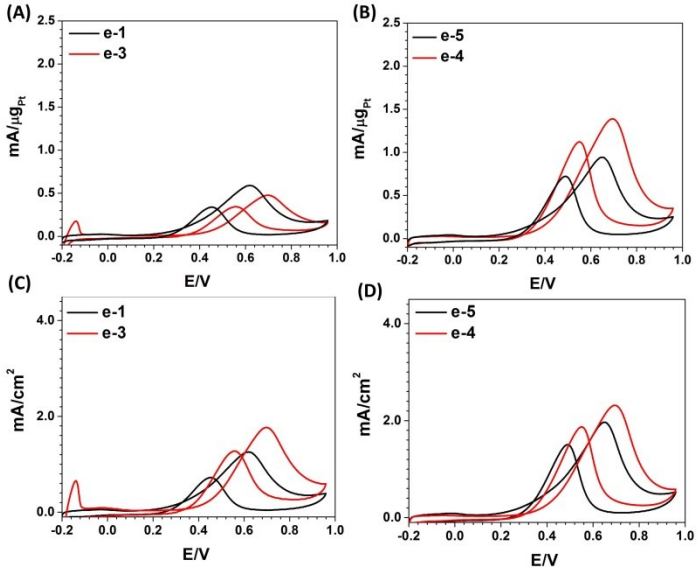

Figure S13. MOR curves of $Pt_{56}Au_{44}$/C in 0.5 M CH_3OH+0.1 M $HClO_4$ based on (A, B) Pt mass and (C, D) active surface area. (e-1, e-5) 260 ºC/O_2 treated with PtAu loading of 25 wt%, (e-3, e-4) 400 ºC/H_2 treated with PtAu loading of 27 wt%. (e-4 and e-5: activated with CV cycling to a higher potential).

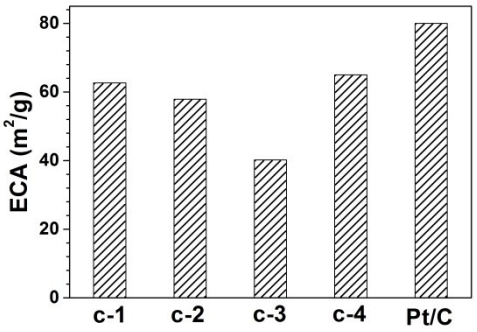

Figure S14. Comparison of electrochemical active area (ECA) for (c-1) 260 ºC/O_2, (c-2) 177 ºC/O_2, and (c-3) 400 ºC/H_2 treated $Pt_{39}Au_{18}Ni_{43}$/C and Pt/C c-4 involves 400 ºC/H_2 treated $Pt_{39}Au_{18}Ni_{43}$/C with cycling to higher potential. (1.39 V)

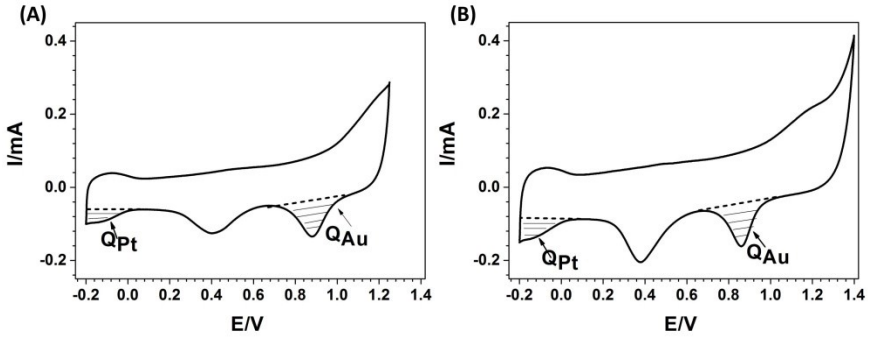

Figure S15. CV curves for (A) Sample c-3, (B) c-4. The total surface concentration of Pt is calculated by integrating the capacity-corrected H_2 underpotential deposition in the range a -0.2 to 0.1 V (Q_{Pt}), which is transferred to cm^2_{Pt} by dividing with 210 μC/cm^2. The relative concentration of Au is calculated by integrating the capacity-corrected Au oxide formation in the range of 0.65 to 1.05 V (Q_{Au}), which is converted to cm^2_{Au} by dividing with 340 μC/cm^2. In this sample, the measured percentage of Pt, Pt/(Pt+Au) was 55% and 60% for Sample c-3 and c-4.

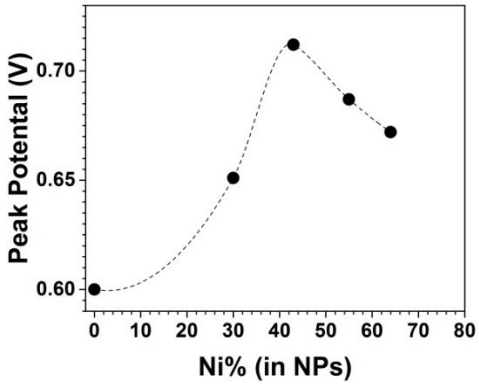

Figure S16. The peak potential in the forward sweep vs. Ni% for the 400 ºC/H_2 treated $Pt_{\sim 40}Au_xNi_{\sim 60-x}$/C.

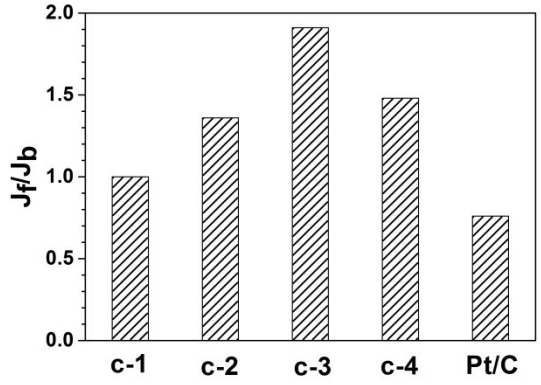

Figure S17. The ratio of forward (J_f) and backward (J_b) peak current for (c-1) 260 ºC/O_2, (c-2) 177 ºC/O_2, and (c-3) 400 ºC/H_2 treated $Pt_{39}Au_{18}Ni_{43}$/C and Pt/C. c-4 involves 400 ºC/H_2 treated $Pt_{39}Au_{18}Ni_{43}$/C with cycling to higher potential (1.39 V).

.

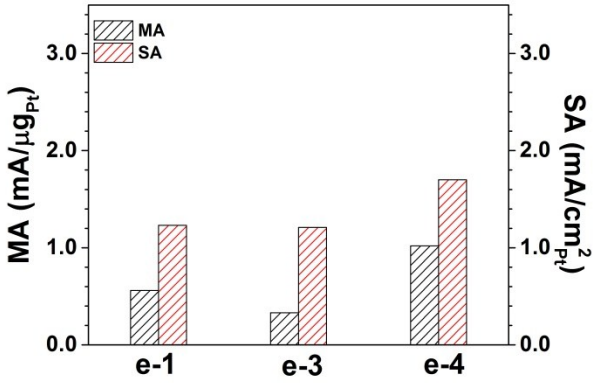

Figure S18. MA and SA at 0.6 V in forward sweeps for (e-1) 260 ºC/O_2 and (e-3, e-4) 400 ºC/H_2 treated $Pt_{56}Au_{44}$/C. ((e-4): activated with CV cycling to a higher potential)

Table S1. Comparison of electrocatalytic MOR activities (optimal) for $Pt_{39}Au_{18}Ni_{43}$/C and other catalysts reported.

catalysts	MA ratio of catalyst vs. Pt/C	SA ratio of catalyst vs. Pt/C	J_f/J_b	electrolyte	References
$Pt_{50}Au_{50}$ particles	-	2.2	~1.1	0.1 M $HClO_4$	[6]
PtNi ribbons	1.5	4	1.14	0.5 M H_2SO_4	[17]
PtNi particles	1.24	1.6	~1.1	0.5 M H_2SO_4	[18]
PtAu nanotubes	1.53	3.33	~1	0.5 M H_2SO_4	[8]
PtZn cubics	-	1.23	1.8	0.1 M H_2SO_4	[64]
PtCu hollow NPs	3.73	4.46	~1	0.5 M H_2SO_4	[65]
$Pt_{39}Au_{18}Ni_{43}$/C	2.5	3.92	1.91	0.1M $HClO_4$	this work

Table S2. XPS peak positions (unit: eV) for (c) as-synthesized, (c-1) 260 ºC/O_2, (c-2) 177 ºC/O_2, and (c-3) 400 ºC/H_2 treated $Pt_{39}Au_{18}Ni_{43}$/C in terms of the deconvoluted XPS peaks, including Ni $2p_{3/2}$(Ⅰ) and $2p_{3/2}$(Ⅱ), Pt^0 $4f_{7/2}$, and $4f_{5/2}$, and Au $4f_{7/2}$ and $4f_{5/2}$, before (BC) and after (AC) potential cycling

XPS peak	Sample c-1	Sample c-2	Sample c-3	Sample c
Ni $2p_{3/2}$ (I) (BC)	854.00	853.50	853.10	853.39
Ni $2p_{3/2}$ (I) (AC)	853.83	853.40	853.22	-
Ni $2p_{3/2}$ (II) (BC)	856.10	856.10	856.50	856.35
Ni $2p_{3/2}$ (II) (AC)	856.87	856.00	855.19	-
Pt^0 $4f_{7/2}$ (BC)	71.65	71.68	71.70	71.80
Pt^0 $4f_{7/2}$ (AC)	71.75	71.70	71.82	-
Pt^0 $4f_{5/2}$ (BC)	74.96	74.98	75.05	75.08
Pt^0 $4f_{5/2}$ (AC)	75.05	75.00	75.21	-
Au $4f_{7/2}$ (BC)	84.38	84.35	84.33	84.52
Au $4f_{7/2}$ (AC)	84.62	84.52	84.52	-
Au $4f_{5/2}$ (BC)	88.05	88.06	88.04	88.24
Au $4f_{5/2}$ (AC)	88.19	88.16	88.17	-

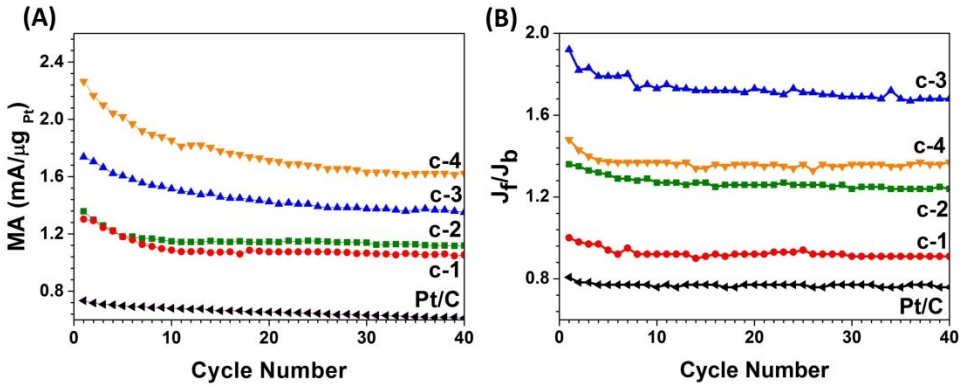

Figure S19. (A) Mass activity at 0.69 V and (B) the ratio of forward and backward peak (J_f/J_b) current vs. cycle number for (c-1) 260 ºC/O_2, (c-2) 177 ºC/O_2, (c-3) 400 ºC/H_2 treated $Pt_{39}Au_{18}Ni_{43}$/C. c-4 involves 400 ºC/H_2 treated $Pt_{39}Au_{18}Ni_{43}$/C after potential cycling to 1.39 V.

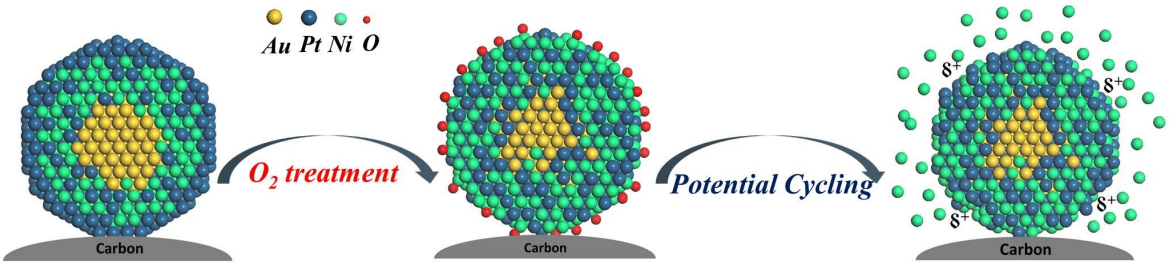

Scheme S2. Schematic illustrations of the reconstruction of $Pt_{39}Au_{18}Ni_{43}$ core-shell NPs in terms of the relative surface enrichment and alloying by thermal treatment under O_2.